JOURNAL OF CATALYSIS **174,** 130–141 (1998)
ARTICLE NO. CA981934

Crystallite Size Determination of Highly Dispersed Unsupported MoS_2 Catalysts

Christophe Calais,* Nobuyuki Matsubayashi,* Christophe Geantet,† Yuji Yoshimura,* Hiromichi Shimada,* Akio Nishijima,* Michel Lacroix,† and Michèle Breysse‡

**National Institute of Materials and Chemical Research, 1-1 Higashi, Tsukuba, Ibaraki 305, Japan; †Institut de Recherches sur la Catalyse, 2, Avenue Albert Einstein, 69626 Villeurbanne Cedex, France; and ‡Laboratoire de Réactivité des Surfaces, 4 Place Jussieu, 75252 Paris Cedex 05, France*

Received May 29, 1997; revised August 21, 1997; accepted October 3, 1997

Crystallite size determination of MoS_2 particles is still a controversial problem fuelling the debate on the morphology of hydrotreating catalysts. The size of MoS_2 crystallites determined from extended X-ray absorption fine structures (EXAFS) is close to 1 nm, whereas TEM picture analysis give an average size of 3 to 4 nm. It is obvious that these techniques have intrinsic strengths and weaknesses and that the results may not be comparable because of these differences. However, it is our intention to obtain a better understanding of these crystallite sizes by studying the dispersed unsupported solids. Various techniques were used: nitrogen adsorption–desorption, X-ray diffraction (XRD), XAFS, TEM, and temperature-programmed reduction (TPR) and the results were compared and discussed. The samples were prepared by thiosalt decomposition or molten salt synthesis. These solids presented different morphologies, the latter method providing higher surface area samples. The specific surface areas varied from 4 to 125 m^2/g and, depending on the method of preparation, microporous and mesoporous solids were obtained. XRD, TEM, and TPR were found to be complementary and coherent methods for determining the size parameter. EXAFS interpretation does not give consistent results due to local reorganization at the periphery of the crystallites. © 1998 **Academic Press**

INTRODUCTION

Crystallite size determination remains a crucial problem in the field of catalysis because a correct interpretation of heterogeneous reaction kinetics requires knowledge about the number of active atoms exposed at the surface. For metal catalysts, the determination of the particle size was achieved by using several techniques such as X-ray diffraction (XRD), high resolution electron microscopy (HREM), selective gas chemisorption, and recently extended X-ray absorption fine structures (EXAFS). However, for highly dispersed catalysts with particle sizes typically smaller than about 10 nm, methods such as XRD may fail to reveal such information, whereas electron microscopy, gas chemisorption, and EXAFS are reliable (1).

Sulfides represent an important class of catalysts due to their industrial use in the hydrotreatment process. In this field, industrial catalysts are composed of molybdenum or tungsten sulfides promoted by Ni or Co supported on alumina. These catalysts are complex because of their highly anisotropic layered structure. They are commonly seen as slabs with an MoS_2-like structure with only a few layers. It is now agreed that the active sites and/or the promoter are located at the edges of the lamellar structure. The determination of the length and the number of fringes is of primary importance. Numerous studies have been devoted to the determination of the particle size of the active sulfide phase using HREM or EXAFS. Both methods give controversial data. Particle size in the range 3–5 nm are generally observed with HREM, while EXAFS data show that the average coordination numbers of molybdenum atoms around molybdenum are smaller than those expected for these particle sizes (2–12). Taking into account this discrepancy, Eijsbouts *et al.* (13) suggested that a fraction of the MoS_2 particles cannot be detected by HREM. There is apparently no other technique that can support either HREM or EXAFS measurements, because chemisorption methods cannot be applied to sulfide catalysts due to the lack of selectivity of the usual probe molecules.

Besides these physical methods, temperature-programmed reduction (TPR) may be an interesting tool for determining the particle size of sulfided materials. This technique is indeed highly sensitive and does not depend on any specific property of the solid under investigation other than its reducibility. On this chemical basis, the H_2S production would be related to the reactivity of surface sulfur anions and, consequently, to the particle size of the sample under study. Such an approach has been recently undertaken using either unsupported or alumina-supported ruthenium sulfide catalysts. For these types of catalysts the TPR profiles usually exhibit three peaks. The combined use of TPR data and a geometrical model has allowed us to distinguish between the H_2S resulting from surface reduction and the H_2S from bulk reduction. As this relative proportion depends

0021-9517/98 $25.00

on the dispersion of the sulfide phase, it was possible to relate peak intensities to particle size. Data have shown that the thus-calculated particle size is in good agreement with the average size experimentally deduced from HREM.

The properties of unsupported catalysts are roughly similar to those of supported systems. Thus, the problem of the interaction between the active phase and the support, which generally involves interactions via O–Mo–S bonds and which may influence the EXAFS data treatments, is avoided with model unsupported solids. The decomposition of ammonium thiomolybdates (ATTM) (14–17) allows the preparation of unsupported MoS_2 with significant textural properties, which may be modified by changing the decomposition temperature. In order to get a completely different texture, we also synthesized MoS_2 according to a new method based on molten salt techniques. Molten salts can be considered an interesting way to prepare poorly organized solids. The bath is generally constituted by a salt with a low melting point. Consequently, relatively low temperatures are necessary and the products may reveal textures with a strong amorphous character. Previous studies related to the behavior of transition metal cations in molten potassium thiocyanate (melting point: 450 K) demonstrated the possibility of synthesizing sulfides (18). Sodium molybdate or molybdenum oxide reacts in thiocyanate melt to precipitate MoS_2 (19, 20).

The objective of this work is to compare estimates of the particle sizes determined from XRD, HREM, EXAFS analyses, and TPR of these amorphous MoS_2 compounds. The accuracy and limitations of each technique are discussed and compared.

EXPERIMENTAL

Catalysts Preparation

Two different routes were taken for the preparation of model unsupported MoS_2. The first one involves the thermal decomposition of ATTM, while the second method concerns the direct synthesis in a molten bath.

Pure ATTM red crystals were prepared by crystallization of a saturated solution of ammonium heptamolybdate in a commercial solution of ammonium sulfide (20% $(NH_4)_2S$) (21). Thermal decomposition of the ATTM precursor was performed by heating the solid to 673 K in a H_2/H_2S 15% gas mixture according to the following reactions:

$$(NH_4)_2MoS_4 \xrightarrow{573\ K} MoS_3 + (NH_4)_2S \qquad [1]$$

$$MoS_3 \xrightarrow{633\ K} MoS_2 + 1/x\ S_x. \qquad [2]$$

Samples resulting from this preparation will be denoted as AT.

The second preparation method involved a reaction between potassium thiocyanide (Aldrich) and molybdenum oxide (Merck). The procedure is similar to the method referred to in (19). The reaction was carried out in a Pyrex tube at 623 K for 48 h and kept under nitrogen flow in order to eliminate the oxygen formed by the reaction. The overall reaction of molybdenum (VI) oxide can be represented by the stoichiometry

$$MoO_3 + 2\,SCN^- \rightarrow MoS_2 + 2\,OCN^- + \tfrac{1}{2}\,O_2. \qquad [3]$$

A black precipitate was obtained. Chemical analysis gave a K content lower than 0.2 wt%. After washing with water in a soxhlet apparatus, sulfidation (4 h under H_2/H_2S 15%) was used to restore the MoS_2 surface. These samples will be referred as MS.

To modify the size of the particles, different activation temperatures were used (673 K $< T <$ 873 K).

BET Area and XRD

The specific surface areas and isotherms of the different samples were determined by nitrogen physisorption at 77 K.

The XRD diffraction patterns of the catalysts were recorded on a Material Analysis Chemical MXP8 diffractometer using Cu$K\alpha$ radiation generated at 45 kV and 60 mA. For all the samples the 2θ range was 10–70° and a scan speed of 2°/min was used. The powdered solids were dispersed in a collodion solution on the sample holder in order to prevent air oxidation during the measurements.

Temperature-Programmed Reduction Analysis

TPR experiments were carried out using conventional TPR equipment. The composition of the product gases was monitored by using a quadrupole mass spectrometer ULVAC, Q150-A. The sample was loaded in a quartz reactor (inner diameter 4.5 mm) and then flushed with nitrogen for 15 min. Reduction of the solid was carried out under a total flow of H_2/N_2 (50% H_2) of 418 cm^3/min with a heating rate of 5 K/min to 1073 K. The weight of the catalyst was in the range 0.2–0.3 g for all the experiments. At the beginning and at the end of each TPR run, the detector was calibrated using a mixture containing 992 ppm of H_2S diluted in nitrogen.

High Resolution Electron Microscopy

High resolution electron microscopy was performed with a JEOL 100 CX instrument fitted with a UHP polar piece. Its resolving power was 0.2 nm. The solids were ultrasonically dispersed in ethanol, and the suspension was collected on carbon-coated grids.

EXAFS Analysis

EXAFS spectra (Mo K-edge) were recorded at the Photon Factory (beam line 10B) of the National Laboratory for High Energy Physics (Tsukuba, Japan). The X-ray emitted by positrons in the storage ring operated at an energy of 2.5 GeV and were monochromatized by a channel cut Si (311) monochromator. The current intensity of the ring was in the range 250–350 mA. The sulfided catalysts were pressed into wafers of adequate thickness x so that $\Delta\mu x =$ 1.0–1.5. For this purpose cellulose was used as a binder. Preparations of the samples and the measurement of the X-ray absorption were carried out under nitrogen. All spectra were recorded at room temperature in the transmission mode. The beam intensity was measured before and after the sample (I_0 and I, respectively) using ionization chambers filled with mixtures of 15% Ar and 85% N_2 for I_0 and 50% Ar and 50% N_2 for I. Fourier transformation of the $k/f(k)$ weighted EXAFS data for $\Delta k = 14$ Å^{-1} $(3 < k < 17)$ was performed to obtain the radial distribution function around Mo. The phase shift and backscattering amplitude were corrected by using the calculated values (22) for Mo as an adsorber and S as a scatterer. The final structural parameters were determined by the curve fitting method on the Fourier filtered data. The detailed analytical EXAFS procedure has been described elsewhere (23, 24). Multiple scattering was taken into consideration in interpreting the EXAFS results by FEFF 6 simulation (22).

RESULTS AND DISCUSSION

Textural Properties of Unsupported MoS_2 Samples

Surface area measurement is a prime indicator of a poorly crystalline state. For nonporous materials these measurements may be related to the particle size. As reported in Table 1, both preparation methods gave solids with high surface areas. The molten salt technique provides samples with surface areas higher than 100 m^2/g; these surface areas are maintained, even for a sulfidation pretreatment performed at a temperature as high as 873 K. In contrast, solids prepared by decomposition of the ATTM precursor sintered rapidly by increasing the decomposition temperature. Our study focused on MS125 and AT50 samples.

TABLE 1

Textural Properties and Nomenclature of the Unsupported MoS_2 Solids

Preparation method	Sulfidation temperature (K)	Sample nomenclature	S_{BET} (m^2/g)	V_p (cm^3/g)	S_t (m^2/g)
ATTM	673	AT50	50	0.07	26
ATTM	773	AT30	30		
ATTM	873	AT20	20		
ATTM	973	AT4	4		
Molten salt	673	MS125	125	0.37	124
Molten salt	773	MS110	110		
Molten salt	873	MS100	100		

Note. (S_{BET}, specific surface area; V_p, porous volume; and S_t, t surface area).

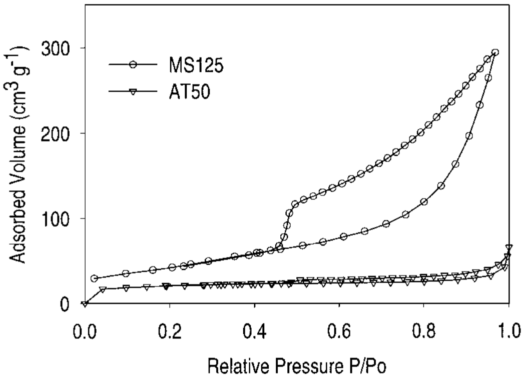

FIG. 1. Nitrogen adsorption–desorption isotherms at 77 K for AT50 and MS125 samples.

Parallel to these area variations, the nitrogen adsorption–desorption isotherms reveal differences in the porosity of the samples. Figure 1 presents the isotherms of the two samples. The MS125 solid exhibits a type IV isotherm according to the nomenclature of the I.U.P.A.C. (25), while the AT sample possesses a type I characteristic for a microporous material. The t-plots presented in Fig. 2 show more precisely how the texture of the samples varies with the preparation method. In this figure, the thickness of the adsorbed volume was calculated according to Halsey's equation in order to account for the observed value of the C constant of the BET equation ($C \sim 50$) (26). For the MS sample, the y-intercept deduced from the linear section is rather small, indicating a very low microporosity; consequently, the t surface area agrees fairly well with S_{BET} measurements as indicated in Table 1. The t-plot of the AT sample confirmed the presence of microporosity and half of its surface area resides inside micropores. Consequently, BET measurements cannot be used for the determination of particle size.

XRD Patterns of the MoS_2 Samples

XRD patterns of the AT50, AT20, AT4 (Fig. 3A), and MS125 samples (Fig. 3B) are characteristic of a poorly crystalline molybdenum disulfide (27). The first diffraction peak

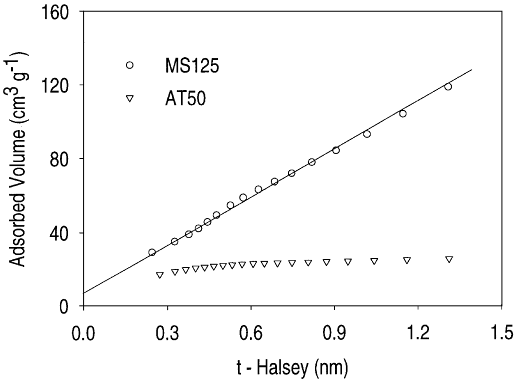

FIG. 2. V_{ads}–t plots for AT50 and MS125 samples.

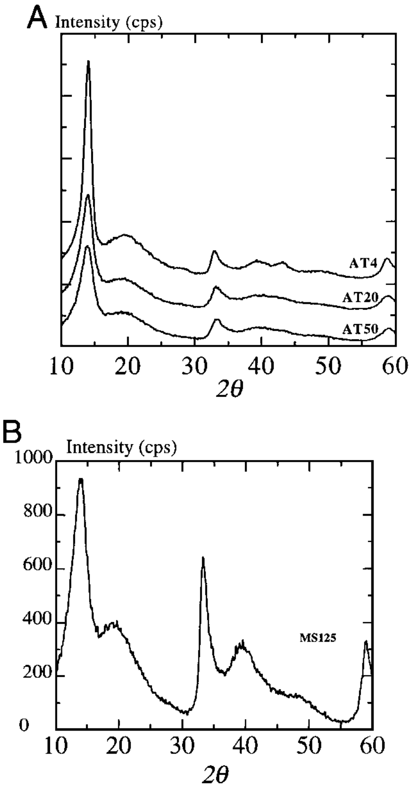

FIG. 3. XRD patterns of AT samples (A) and MS125 sample (B).

corresponds to the (002) plane and determines the height of the crystallite. The width of this line indicates (from the Scherrer formula) that the average correlation distance along the *c*-axis is approximately 5 layers (see Table 2).

A broad envelope, beginning approximately at $2\theta = 30^\circ$ and continuing above 60°, contains several peaks. Peaks at about 32° correspond to (100) and (101) planes and are indicative of the length of the slab. The AT samples present a lower order in the basal directions (length <10 nm in all cases) than in the MS direction (length >10 nm) (see Figs. 3A and 3B). Precise determination of the length using Scherrer formula is not possible because of the overlap of the peaks and the presence of random defects characterized by a rapid increase in the diffracted intensity followed by a slow decrease (28).

As shown by the BET measurement, the sulfidation temperature substantially influences the texture of the AT materials. For these solids, the XRD patterns show that sintering occurs with an increase in the sulfidation temperature because the intensity of the (002) peak grows and sharpens (see Table 2). In contrast, the diffraction lines at about 32° are slightly affected by the sulfidation treatment.

TABLE 2

Average Number of Layers Deduced from (002) Line Broadening of Unsupported MoS_2

Preparation method	Thiosalt decomposition				Molten salt
Samples	AT50	AT30	AT20	AT4	MS125
Number of layers from XRD	4	5.8	6.5	10	5

High Resolution Electron Microscopy

HREM studies of the catalysts revealed the presence of structures typical of the layered MoS_2 phase. The lattice fringes observed have a spacing of about 0.6 nm compared to a 0.615 nm spacing of the (002) basal planes of MoS_2. Catalysts obtained from ATTM decomposition are twisted in closely packed groups of relatively small slabs (Fig. 4). Statistics performed on several pictures (up to 10) gave an average length of 4 nm and an average number of layers of 4 for AT50 sample (Figs. 5A and 5B). These results are similar to those presented for identically prepared unsupported catalysts (29).

Sample AT4 (Fig. 6) presents a mixture of relatively small particles and of sintered particles. Length and stacking vary from 3 to 50 nm and from 3 to 16 layers, respectively. The XRD pattern (see Fig. 3A) reflects the increase in the number of layers, but the modification of the length of the slabs is apparently small. This discrepancy was already reported by Inamura and Prins (30), who suggested that winding and bending structures are responsible for this effect.

Molten salt preparation gives rise to a completely different texture; the MoS_2 particles have a loose structure with long separated crystallites (Fig. 7). Their average length is 12.6 nm with an average stacking of 5 (Figs. 5A and 5B). These data are in good agreement with those obtained from the XRD patterns.

From the length and stacking deduced from TEM statistics, it is possible to calculate the geometrical surface area of the sample on the basis of hexagonal crystallites. The formula

$$S_f = (1.3L^2 + 18.45nL - 3.75I)37.6/(nM_t) \quad (\text{in m}^2/\text{g})$$

is proposed, where n represents the average stacking number, L the average length, and M_t the total number of Mo atoms in a crystallite. Calculated geometrical surface areas are equal to 374 and 209 m^2/g for the ATM/50 and MS/125 solids, respectively. In the latter case, almost 60% of the geometrical surface area is observed by BET whereas for the ATM sample only 13% is revealed by nitrogen physisorption, suggesting a dense packing of small crystallites as observed by TEM.

Temperature-Programmed Reduction

TPR profiles of the AT and MS samples are presented in Fig. 8. They exhibit a first sharp peak at around 400 K and a broad area of desulfurization between 473 and 873 K. Above this temperature, H_2S production rises sharply. The limited performance of the furnace does not allow a

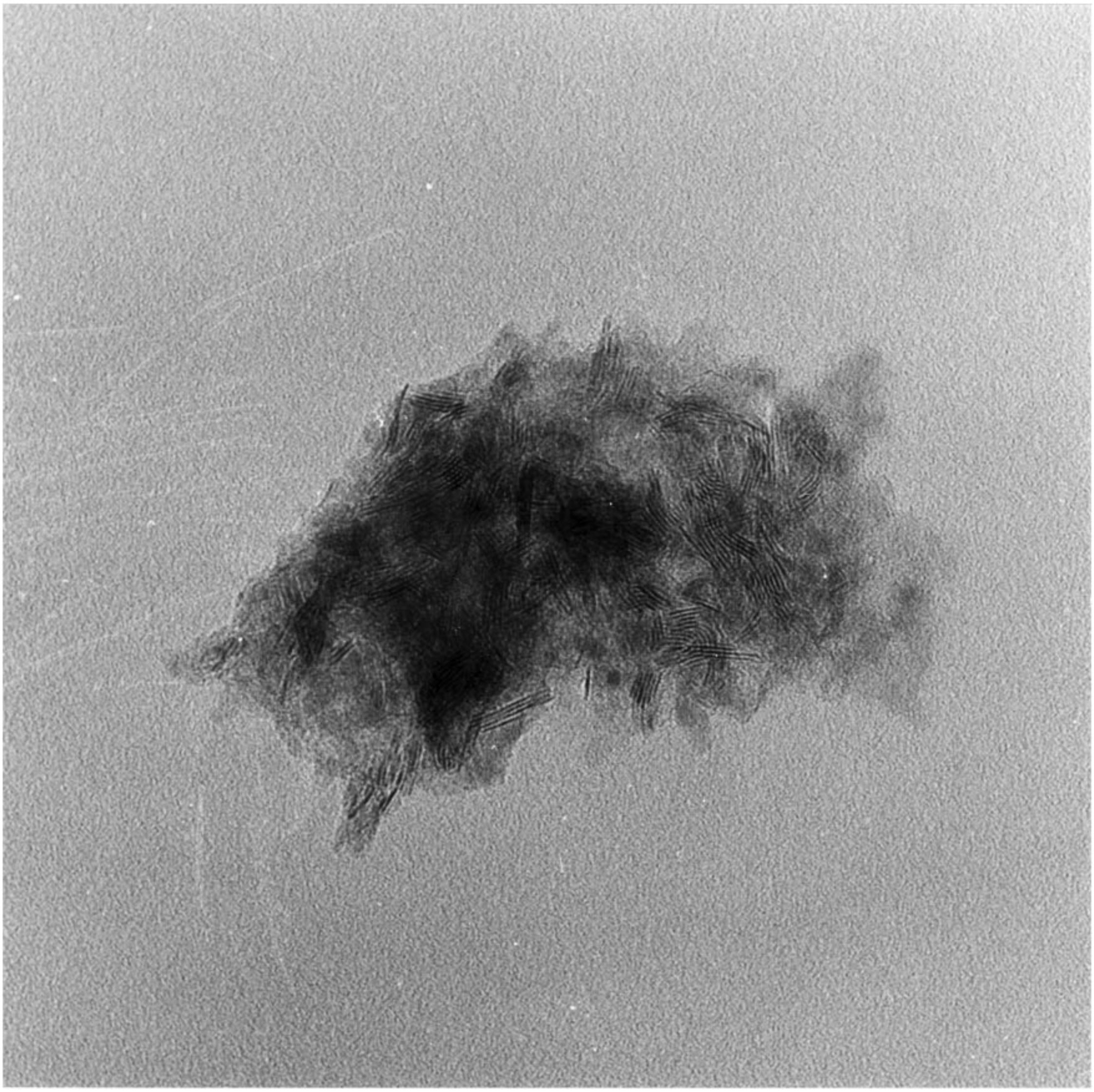

FIG. 4. HREM picture of AT50 sample ($G = 1$ M).

complete reduction of the solids. For a quantitative analysis, the TPR profiles were divided into three regions shown in Table 3. It appears from these values that, for the AT series, the higher the surface area, the more reducible the solid is. Surprisingly, this is not the case for the MS125 sample, which loses only a small amount of sulfur with respect to its high surface area.

TPR has been used in the study of supported sulfide catalysts (31–33) and also to a lesser extent for unsupported catalysts (34–36). If the support interacts weakly with H_2S, then direct correlation can be made between H_2S production and the nature of the different peaks. If it is possible to quantify the reducibility of the sample by a convenient geometrical model, the size of the particle may also be obtained. Such an approach was successfully used in the cases of unsupported and supported ruthenium disulfide, and it was shown that the particle size can be estimated from the TPR profiles (37). A geometrical model has been also proposed for MoS_2-based hydrotreating catalysts, describing the active phase as small slabs with different shapes dispersed on the support (38). A theoretical approach (Gibbs–Curie–Wulf law) predicted that the hexagonal shape is the most stable form (39) as depicted in Scheme 1. If we consider this

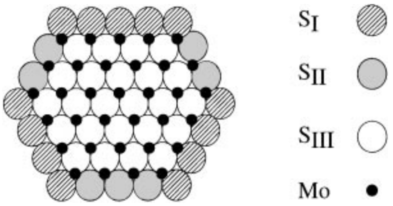

SCHEME 1. Geometrical modeling of a single slab of MoS_2.

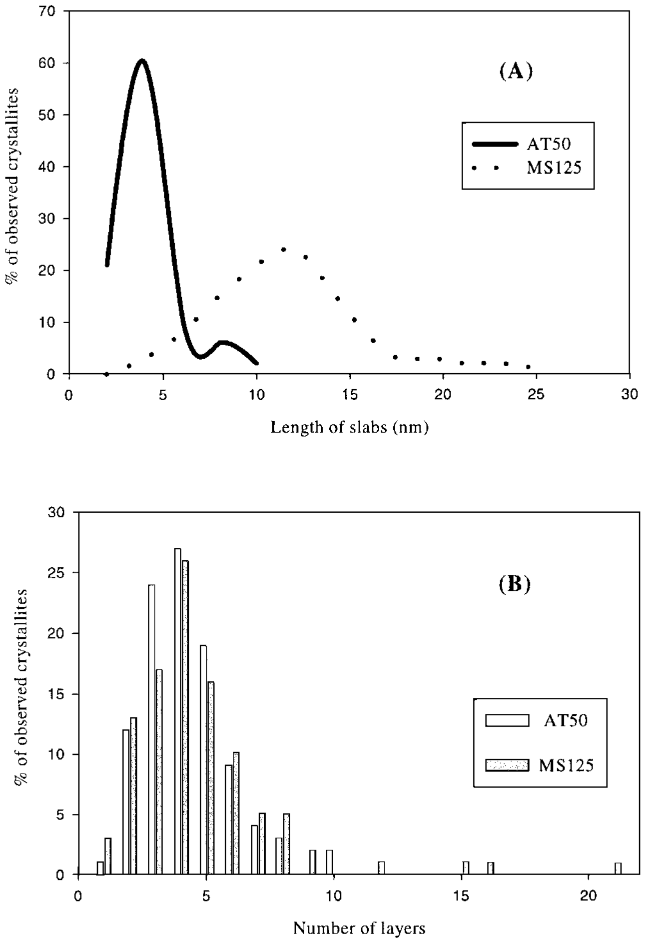

FIG. 5. Distribution of the length of the crystallites (A) and of the number of layers (B) for AT50 and MS125 samples.

hexagonal crystallite with L Mo atoms on one edge of the hexagon, the total number of Mo atoms, M_t, the number of edge Mo atoms, M_e, and the number of sulfur ions in the basal plane (i.e., excluding those on the edges), S_b, are easily deduced from the following equations:

$$M_t = 3L^2 - 3L + 1 \quad [4]$$

$$M_e = 6(L - 1) \quad [5]$$

$$S_b = 6(L - 1)^2. \quad [6]$$

The edge sulfur atoms are not equivalent, because their local environment is different. S_I and S_{II} sulfur types are coordinated to 1 and 2 molybdenum atoms, respectively (38). According to this notation all the S_b atoms can be indexed as S_{III}. Formulae for the edge sulfurs, $S_e = (S_I + S_{II})$, S_I and S_{II}, are then given by Eqs. [7], [8], and [9],

$$S_e = 6(2L - 1) \quad [7]$$

$$S_I = 6L \quad [8]$$

$$S_{II} = 6(L - 1), \quad [9]$$

and consequently $S_I/S_T = 1/L$. In such a model, the complete coordination of Mo atoms leads to overstoichiometric slabs MoS_{2+x} with $x = 2[(3L^2 + 6L + 3)/(3L^2 + 3L + 1) - 1]$.

This schematic model does not reflect the real surface of such catalysts but may provide information about the fraction of the different ions present on the crystallite. According to the experimental data, the TPR technique reveals the presence of various sulfur species whose reactivity is related to their chemical environment. For molybdenum sulfide based systems, three reduction zones are observed in either the supported (29) or the unsupported states (35). Due to the activation process used, a complete sulfidation is realized, and overstoichiometric compounds MoS_{2+x} are obtained (34, 40). In a previous work, a stoichiometry of $MoS_{2.27}$ was found for a sample similar to AT50 (40). The first peak was related to a weakly bonded sulfur or extra sulfur (so-called S_x according to Mangnus *et al.* (41)). In fact, charge neutrality of the surface requires the presence of chemisorbed H_2S or SH groups that might be related to these easily removable species. The second broad area (between 473 and 873 K) can be related to the reduction of one part of the surface anions located at the edges of the crystallites, and we assume that it corresponds to a complete removal of sulfur of S_I type, i.e., sulfur ions coordinated to one Mo ion. The third peak corresponds at first to the removal of S_{II} and S_{III} sulfur atoms belonging to the edges and to the basal planes and finally to the sulfur from the bulk. At the beginning of this last reduction step, the stoichiometry of the solid is MoS_2. It is evident that the TPR profile is related to the size of the particles, small crystallites being much more reducible than larger ones. It can be seen that the AT preparation gives rise to much more reducible catalysts than MS samples except for the AT4 solid sulfided at 973 K. Such an effect indicates that different sizes of particles are achieved depending on the preparation methods and sintering processes used. The relative proportion of surface atoms S_x and S_I atoms is deduced from the amount of H_2S removed in regions I and II (surface S) and is assumed to correspond to x in MoS_{2+x} formula. Thus, the

TABLE 3

Amounts of Sulfur Removed during the TPR Experiment

	H_2S removed in 10^{-6} mol/g				
		Surface S			
Catalyst	S_x ($T < 473$ K)	473 K $< T <$ 873 K	$T > 873$ K	Total	S/Mo
AT50	349	1493	468	2310	2.29
AT30	175	1204	561	1940	2.22
AT20	180	922	339	1440	2.18
AT4	48	561	200	810	2.01
MS125	103	573	362	1040	2.11

Note. S/Mo ratios are calculated from $x = 2*$ (S_x + Surface S)/12495. x is the overstoichiometry in MoS_{2+x}.

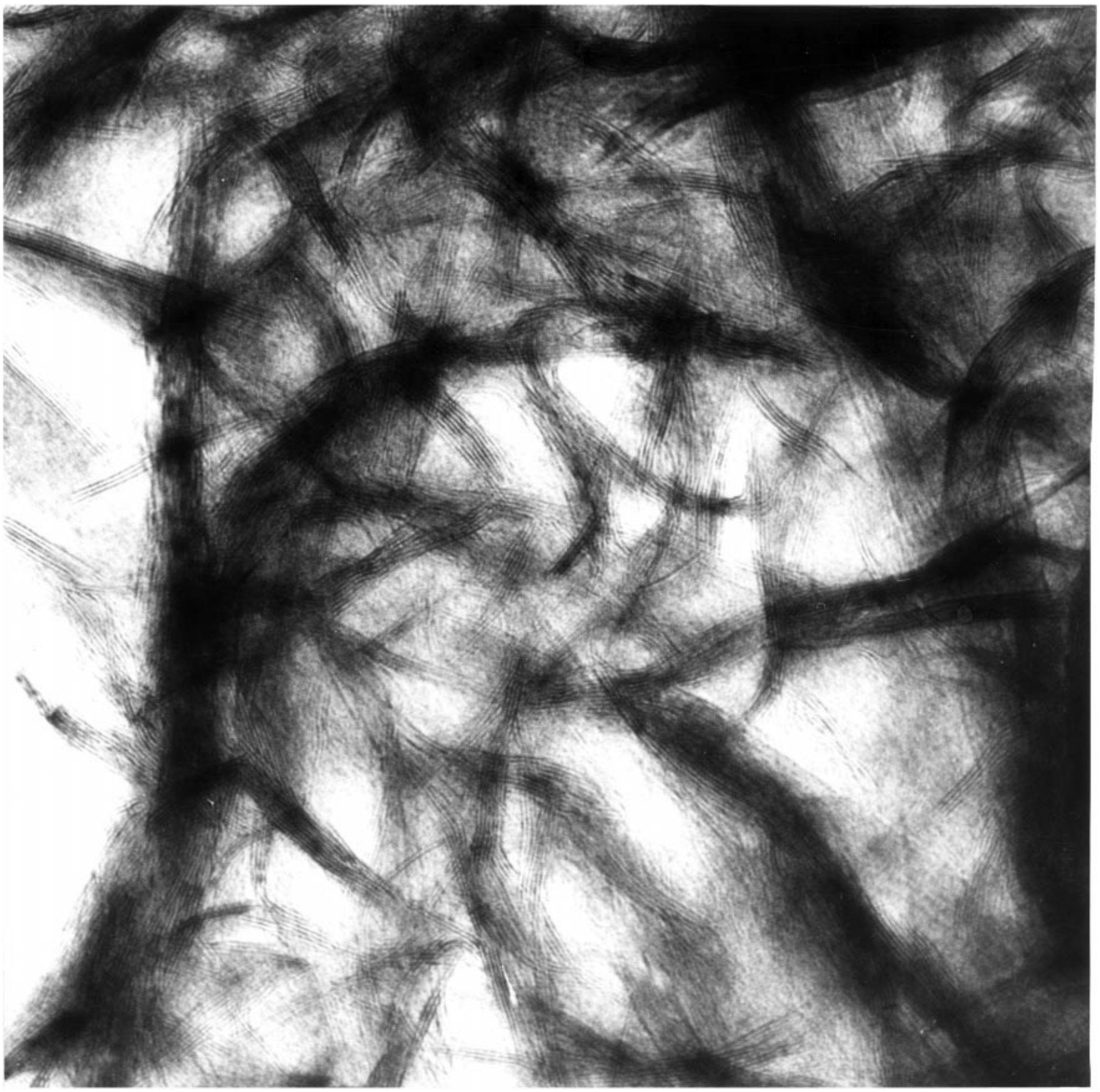

FIG. 6. HREM picture of AT4 sample ($G = 1$ M).

stoichiometry S/Mo of the solids can be deduced (see Table 4). According to the geometrical model, $(S_x + S_I)/S_T = 1/L$, S_T being equal to the H_2S production of the two regions S_x and $S_I + 12495\ 10^{-6}$ mol/g. This L value leads to the crystallite size, expressed as the length of the diagonal of the hexagonal slab ($d = 2(L - 1)\ 0.32$ in nm). The results reported in Table 4 are in fairly good agreement with the particle size determined by HREM.

TABLE 4

Crystallite Sizes Deduced from TPR Profiles

Catalyst	L	d_{TPR} (nm)
AT50	8	5.1
AT30	9	5.8
AT20	11	7.0
AT4	20	12.8
MS125	18	11.5

Note. L corresponds to the number of Mo atoms at the edge of an hexagonal crystallite.

EXAFS Measurements

This work represents the first attempt to measure EXAFS of unsupported dispersed sulfides. All the spectra exhibit two notable peaks corresponding to Mo–S (at 0.242 nm) and Mo–Mo (at 0.316 nm). Figure 9 represents the Fourier Transform EXAFS of AT50 and MS125 samples and of crystalline MoS_2. Figure 10 shows the result of a FEFF calculation performed by using the structure of MoS_2 crystal to estimate the multiple scattering effects. The relative contribution of each scattering is indicated in Fig. 10. A third peak, corresponding to the scattering of the third Mo neighbors

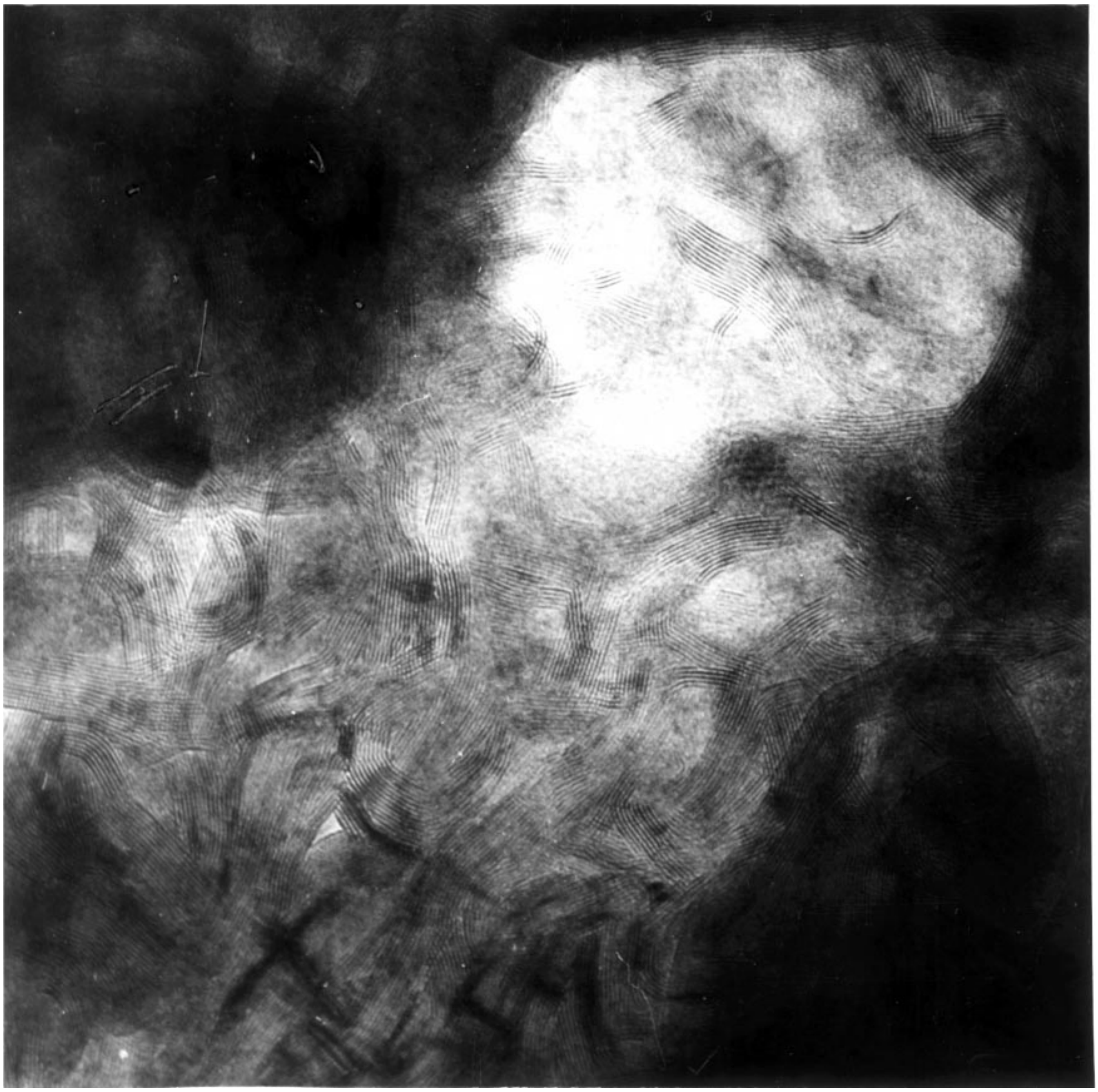

FIG. 7. HREM picture of MS125 sample ($G = 1$ M).

(Mo–Mo 0.632 nm), can also be observed. The results of the FEFF calculation show that this peak mainly consists of multiple scattering. This is a "focusing" effect, which results in an anomalously high magnitude for the third Mo–Mo shell (42). It should be noted that this peak does not reflect Mo–Mo between layers (0.641 nm).

This multiple scattering effect, caused by the unique alignment of the Mo atoms, is indicative of a large order in the unsupported samples. At room temperature, this is usually not visible on supported samples except in the case of high temperature sulfided samples (40). To discuss the EXAFS results quantitatively, the average coordination numbers of sulfur (N(S)) and molybdenum (N(Mo)) around molybdenum have been calculated by curve fitting of the Fourier filtered data in the range $k = 3$–17 Å^{-1}, using the MoS_2 crystal as a standard. The fitting formula is given by

$$\chi(k) = \mathrm{Redfac} \sum N_j |\mathrm{FEFF}_j(k)| \exp\left(-2\sigma_j^2 k^2\right) \exp(-2R_j/\lambda) \times \sin(2kR_j + \phi_{\mathrm{FEFF}_j}(k) + \phi_{\mathrm{c}j}(k))/kR_j^2, \quad [10]$$

where λ is a mean free path and Redfac is a total central atom loss factor, which are given by FEFF. Backscattering amplitudes and phase shifts were calculated using theoretical values $|\mathrm{FEFF}(k)|$, $\phi_{\mathrm{FEFF}}(k)$, and $\phi_{\mathrm{c}}(k)$ obtained by FEFF. k is given by

$$k = (2m(E - E_{\mathrm{temp}} - \Delta E_{\mathrm{o}}))^{1/2}/\hbar, \quad [11]$$

where E_{temp} is threshold energy temporally determined from the inflection point of an edge shape. ΔE_{o} is a fitting parameter, but the results were within 3–5 eV.

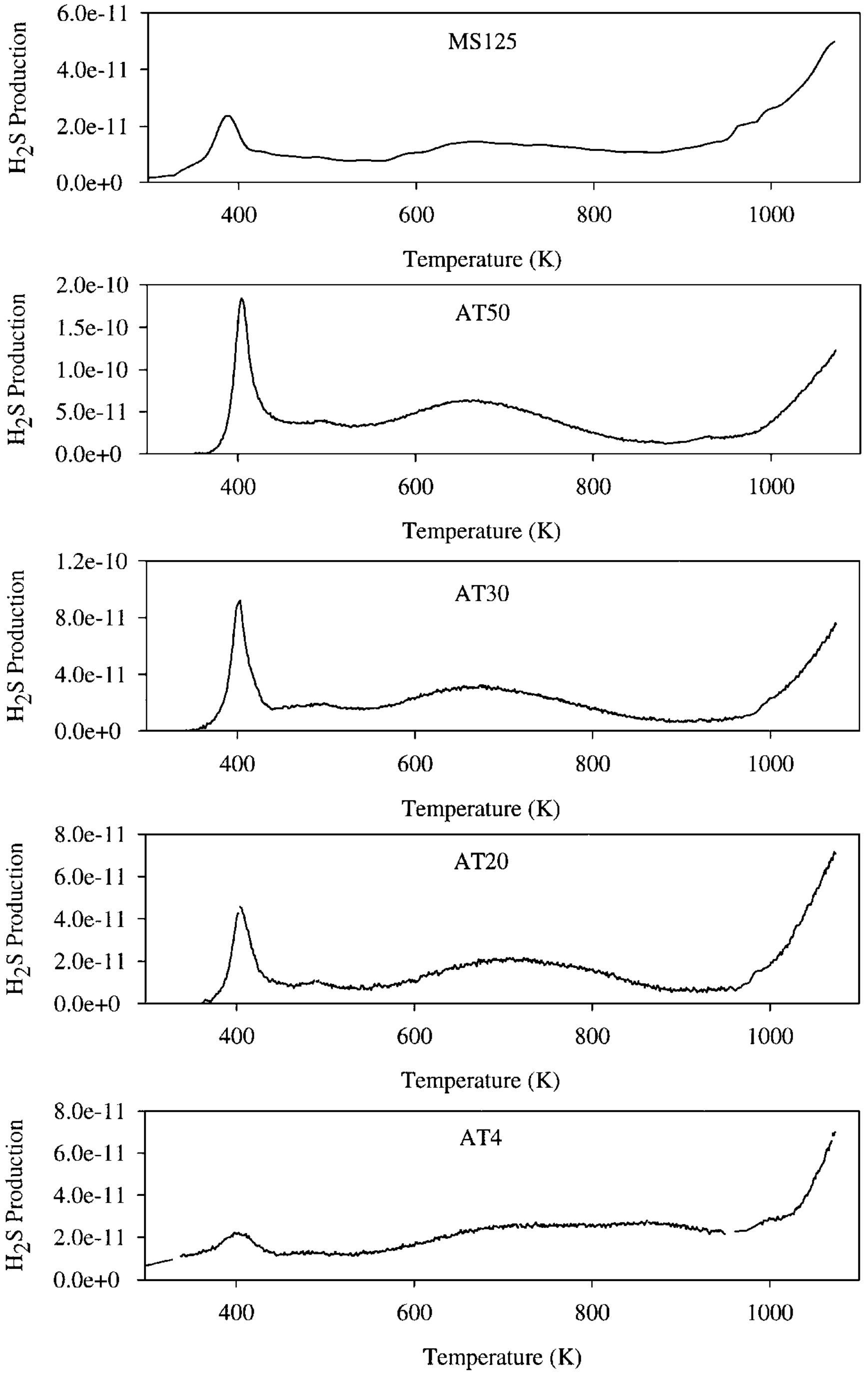

FIG. 8. TPR profiles of AT and MS125 samples.

The structural parameters, N, R, and σ, as well as the residual value R_f were determined as shown in Table 5,

$$R_f = \left(\sum (Y - Y_c)^2 \Big/ \sum Y^2\right)^{1/2}, \qquad [12]$$

where Y is experimental $k^3\chi(k)$ and Y_c is $k^3\chi(k)$ calculated by the fitting formula. Errors of R, N, and σ^2 were estimated to be ± 0.0002 nm, ± 0.2 and $\pm 0.3\ 10^{-5}$ nm^2, respectively, by repeated measurements.

The average number of sulfur neighbors $N(S)$ is close to six in the case of unsupported catalysts. This indicates that the first shell of the molybdenum atoms is well resolved by EXAFS. This value is indicative of a complete sulfidation of the catalysts. Supported catalysts give $N(S)$ values in the range $1.5 < N(S) < 4.5$ (12, 43) depending on the nature

TABLE 5

Structural Parameters from Mo *K*-Edge EXAFS of Unsupported MoS_2 Catalysts for Mo–S and Mo–Mo Coordinations

Catalyst	R(S) nm	N(S)	σ^2(S) 10^{-5} nm^2	R(Mo) nm	N(Mo)	σ^2(Mo) 10^{-5} nm^2	R_f
Single crystal	0.241(8)	6.0	2.3	0.316(0)	6.0	3.4	0.075
AT50	0.241(6)	6.5	2.9	0.316(3)	4.0	4.1	0.082
AT20	0.241(7)	6.7	3.1	0.315(6)	4.4	4.4	0.094
AT4	0.241(4)	6.6	2.8	0.315(7)	4.6	4.4	0.090
MS125	0.241(5)	6.3	2.8	0.315(2)	4.5	4.5	0.072
MS110	0.241(6)	6.4	3.0	0.315(0)	4.4	4.4	0.090
MS100	0.241(8)	6.3	2.8	0.315(1)	4.6	4.5	0.079

Note. Estimated errors: $R \pm 0.0002$ nm, $N \pm 0.2$, $\sigma^2 \pm 0.3 \times 10^{-5}$ nm^2.

of the support, the preparation method, and the thermal treatment used. N(Mo) coordination numbers are smaller than 6 ($4 < N(\mathrm{Mo}) < 5$). This parameter decrease is even more pronounced on supported samples; the N(Mo) values are varying in the range 1 to 3 (44–46). Table 5 shows that the N(Mo) values increase slightly when the surface area decreases.

From the geometrical model, an average coordination number of Mo–Mo can be deduced from the size of the particles (47). According to our formulation, the value of N(Mo) is then equal to

$$N(\mathrm{Mo}) = \frac{24(L-1) + 36\sum_{i=1}^{L-2} i}{1 + 6\sum_{i=1}^{L-1} i} \quad \text{for } L \geq 2. \qquad [13]$$

The coordination numbers obtained experimentally from EXAFS ($N(\mathrm{Mo}) = 4.0$–4.6 (see Table 5)) correspond to a number of Mo atoms per slab in the range $L = 3$, i.e., particle sizes close to 2 nm. EXAFS reflects the general trend of the sintering effect since N(Mo) rises with the size of the particles determined by HREM and TPR. However, the N(Mo) remains low even for particles larger than 10 nm. The argument that this distance is indicative of the mean size of MoS_2 subdomains is used in the literature for the description of supported samples (12). Another interpretation was given by Startsev and Kochubei, who suggested that "outer" Mo atoms localized on the periphery of MoS_2 slabs are not observed by EXAFS because of the high Debye–Waller factors (48). The motion of the atoms in the surface regions of the small slabs induces disorders accompanied by asymmetric pair correlation function and/or anharmonic vibration potential (49). These effects would greatly contribute to the reduction of the EXAFS amplitude. Such effects would increase with decreasing particle size. Clausen *et al.* (1) demonstrated the importance of this phenomenon in the case of copper particles on silica by using molecular dynamic simulation to estimate the distribution of distances.

In order to obtain another representation of the slabs with the EXAFS, we then considered the local structure (R and σ) around Mo at the periphery of the layer to be different from that inside it. Therefore, we separated the EXAFS signal into edge site (^{e}S, ^{e}Mo) and bulk contributions (S_{cry}, Mo_{cry}), the latter being similar to crystalline MoS_2. The

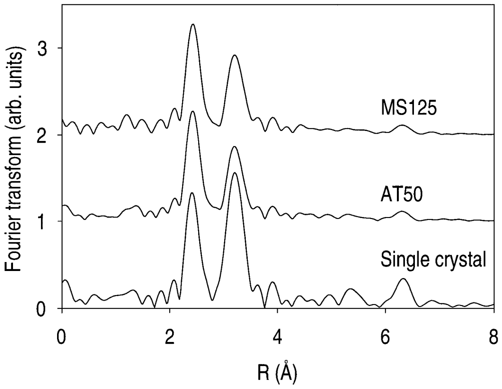

FIG. 9. Fourier transformed EXAFS of MS125, AT50 samples, and crystalline MoS_2.

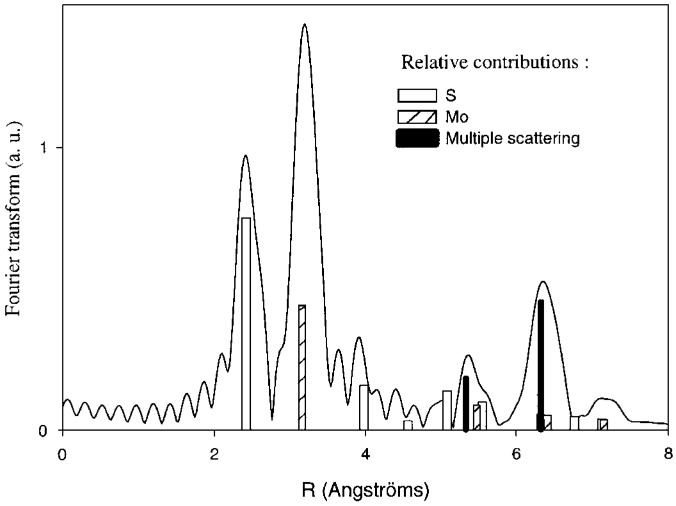

FIG. 10. Fourier transformed EXAFS simulated by FEFF with relative contribution of each scattering.

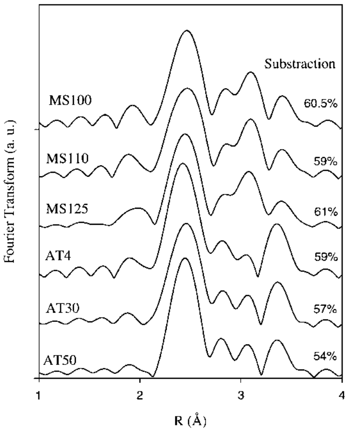

FIG. 11. Fourier transforms of residual $k^3X(k)$ after subtracting contribution of MoS_2 crystalline.

fitting conditions are

$$R(S_{cry}) = 0.2417\ \text{nm}, \quad R(Mo_{cry}) = 0.316\ \text{nm},$$
$$N(S_{cry}) = N(Mo_{cry}), \quad N(S_{cry}) + N(^{e}S) = 6,$$
$$\sigma^2(S_{cry}) = 3.5 \times 10^{-5}\ \text{nm}^2,$$
$$\sigma^2(^{e}Mo) = \sigma^2(Mo_{cry}) = 2.8 \times 10^{-5}\ \text{nm}^2.$$

The fitting procedure gave two different $R(^{e}Mo)$ around 0.31 and 0.34 nm for MS and AT samples, respectively. Therefore, we subtracted the contribution of crystalline MoS_2 from the original EXAFS spectra. Figure 11 shows Fourier transforms of residual $[k/f(k)] \cdot \chi(k)$ by subtracting (in the range 50–60%) and normalizing the Mo concentration. The resulting Fourier transform ought to reflect the local structure around Mo on edge sites. An Mo–S peak is located at 0.241 nm, similar to crystalline or bulk MoS_2. Two remarkable Mo–Mo peaks located at 0.309 and 0.336 nm in MS and AT preparations, respectively, are observed. The first one can be related to a shortened Mo–Mo distance in MoS_2. The second distance cannot be attributed to a characteristic distance in crystalline molybdenum sulfides. This suggests that a specific structure is created, with the AT preparation method, at the periphery of the crystallites of MoS_2.

CONCLUSION

It is obvious that the various techniques described in this work have intrinsic strengths and weaknesses, and the results may not be comparable because of these differences (50). However, a better understanding of the crystallite size of sulfide catalysts can be obtained from studying of dispersed unsupported solids. In addition to the classical method of preparation, the molten salt method provided a new way of synthesizing unsupported molybdenum disulfide with a texture different from that obtained by conventional methods. As a result, the inability of BET measurements to determine crystallite sizes could be demonstrated. Due to the anisotropy of MoS_2, the length and number of layers are used to describe the particles. XRD and HREM give similar distances along the *c*-axis, but the length depends on the preparation method. In fact, the images observed by HREM include defects such as curvatures, which are not observed by XRD (limited by coherent domains). In our study, we introduced the measurement of length parameter by the TPR technique. This quantitative interpretation gave results in good agreement with HREM results. These three techniques give a consistent estimate of the structural parameters. The fact that a chemical probe (H_2), which intervenes in the catalytic process, leads to particle sizes close to those obtained with HREM suggests that bent MoS_2 particles which affect EXAFS and XRD do not or only weakly contribute to catalysis. As observed in the case of supported catalysts, crystallite sizes calculated from EXAFS results are much smaller than those observed by HREM. Apart from the effect of bent structures which are not dominant, we ascribe this to a strong structural disorder of the periphery of the MoS_2 particles. It was suggested for supported catalysts that small particles, stabilized by the support and invisible by HREM, might exist. For unsupported materials, such a hypothesis should be rejected, and we can assume that, as in our case, EXAFS cannot precisely describe the particles present on the surface of hydrotreating catalysts for the purpose of a structure–activity correlation.

ACKNOWLEDGMENTS

The XAFS measurements were performed under the approval of the Photon Factory Program Advisory Committee (Proposal 92-G 195) in the National Laboratory for High Energy Physics. C.C. is indebted to JISTEC and the Science and Technology Agency for a research fellowship and C.G. thanks the Japan Industrial Technology Association for funding. N.M. is indebted to CNRS for a temporary research position.

REFERENCES

1. Clausen, B. S., Grabek, L., Topsøe, H., Hansen, L. B., Stoltze, P., Norskov, J. K., and Nielsen, O. H., *J. Catal.* **141**, 368 (1993).
2. Delannay, F., *Appl. Catal.* **16**, 135 (1985).
3. Mauchaussé, C., Mozzanega, H., Turlier, P., and Dalmon, J. A., *in* "Proceedings, 9th International Congress on Catalysis, Calgary, 1988" (M. J. Phillips and M. Ternan, Eds.), Vol. 2, p. 775. Chem. Institute of Canada, Ottawa, 1988.
4. Ramirez, J., Fuentes, S., Diaz, G., Vrinat, M., Breysse, M., and Lacroix, M., *Appl. Catal.* **52**, 211 (1989).
5. Breysse, M., Cattenot, M., Decamp, T., Fréty, R., Gachet, C., Lacroix, M., Leclerq, C., de Mourgues, L., Portefaix, J. L., Vrinat, M., Houari, M., Grimblot, J., Kasztelan, S., Bonnelle, J. P., Housni, S., Bachelier, J., and Duchet, J. C., *Catal. Today* **4**, 39 (1988).
6. Payen, E., Hubault, R., Kasztelan, S., Poulet, O., and Grimblot, J., *J. Catal.* **147**, 123 (1994).
7. Topsøe, H., and Clausen, B. S., *Catal. Rev.* **26**, 416 (1990).
8. Clausen, B. S., Topsøe, H., Candia, R., Villadsen, J., Lengeler, B., Als-Nielsen, J., and Christiansen, F., *J. Phys. Chem.* **85**, 3868 (1981).

9. Bouwens, S. M. A. M., Prins, R., de Beer, V. H. J., and Koningsberger, D. C., *J. Phys. Chem*. **94**, 3711 (1990).
10. Louwers, S. P. A., and Prins, R., *J. Catal.* **133**, 94 (1992).
11. Louwers, S. P. A., and Prins, R., *J. Catal.* **139**, 525 (1993).
12. Shimada, H., Matsubayashi, N., Saito, Yoshimura, Y., Imamura, M., Kameoka, T., and Nishijima, A., *Catal. Lett.* **20**, 81 (1993).
13. Eijsbouts, S., Heinerman, J. J. L., and Elzerman, H. J. W., *Appl. Catal.* **105**, 53 (1993).
14. Tauster, S. J., Pecoraro, T. A., and Chianelli, R. R., *J. Catal.* **63**, 515 (1980).
15. Vrinat, M., Lacroix, M., Breysse, M., and Fréty, R., *Bull. Soc. Chim. Belg.* **93**, 697 (1984).
16. Liang, K. S., Hughes, G. J., and Chianelli, R. R., *J. Vac. Sci. Technol.* **A**(2), 991 (1984).
17. Roxlo, C. B., Daage, M., Ruppert, A. F., and Chianelli, R. R., *J. Catal.* **100**, 176 (1986).
18. Kerridge, D. H., *in* "Advances in Molten Salt Chemistry," Vol. 3, Chap. 5. Plenum, New York, 1945.
19. Kerridge, D. H., and Walker, S. J., *J. Inorg. Nucl. Chem*. **39**, 1579 (1977).
20. Geantet, C., Kerridge, D. H., Decamp, T., Durand, B., and Breysse, M., *Mater. Sci. Forum* **73–75**, 693 (1991).
21. Diemann, E., and Müller, A., *Coord. Chem. Rev.* **10**, 79 (1973).
22. Rehr, J., Mustre de Leon, J., Zabinsky, S. I., and Albers, R. C., *J. Am. Chem. Soc.* **113**, 5135 (1991).
23. Sakane, H., Miyanaga, T., Watanabe, I., Matsubayashi, N., Ikeda, S., and Yokoyama, Y., *Jpn. J. Appl. Phys.* **32**, 4641 (1993).
24. Matsubayashy, N., Tamayama, M., Shimada, H., Sato, T., Yoshimura, Y., Mori, Y., Kawamata, H., Abe, M., Ogino, K., and Nishijima, A., *Sekiyu Gakkaishi* **37**, 594 (1994).
25. Sing, K. S., Everett, D. H., Haul, R. A. W., Moscou, L., Pierotti, R. A., Rouquerol, J., and Siemieniewska, T., *Pure Appl. Chem*. **57**, 603 (1985).
26. Duchet, J. C., Tilliette, M. J., and Cornet, D., *Catal. Today.* **10**, 507 (1991).
27. Chianelli, R. R., Prestige, E. B., Pecoraro, T. A., and DeNeufville, J. P., *Science* **203**, 1105 (1979).
28. Drits, V. A., and Tchoubar, C., "X-ray Diffraction by Distorted Lamellar Structures," Springer-Verlag, Berlin, 1990.
29. Del Valle, M., Yanez, M. J., Avalos-Borja, M., and Fuentes, S., *in* "Hydrotreating Technology for Pollution Control" (L. Ocelli and R. Chianelli, Eds.), p. 47. Dekker, New York, 1996.
30. Inamura, K., and Prins, R., *J. Catal.* **147**, 515 (1994).
31. Scheffer, B., Dekker, N. J. J., Mangnus, P. J., and Moulijn, J. A., *J. Catal.* **121**, 31 (1990).
32. McGarvey, G. B., and Kasztelan, S., "Studies in Surface Science and Catalysis," Vol. 73, 3 (K. J. Smith and E. C. Sanford, Eds.), Elsevier, Amsterdam, 1992.
33. Nag, N. K., Fraenkel, D., Moulijn, J. A., and Gates, B. C., *J. Catal.* **66**, 162 (1980).
34. Kathold, D. J., and Weller, S. W., *J. Catal.* **95**, 455 (1985).
35. Breysse, M., Frety, R., Vrinat, M., Grange, P., and Genet, M., *Applied Catal.* **12**, 165 (1984).
36. Li, X. S., Xin, Q., Guo, X. X., Grange, P., and Delmon, B., *J. Catal.* **137**, 385 (1992).
37. Geantet, C., Calais, C., and Lacroix, M., *C. R. Acad. Sci. Paris* **315**, 439 (1992).
38. Kasztelan, S., Toulhouat, H., Grimblot, J., and Bonnelle, J. P., *Appl. Catal.* **13**, 127 (1984).
39. Toulhouat, H., and Kasztelan, S., *in* "Proceedings, 9th International Congress on Catalysis, Calgary, 1988" (M. J. Phillips and M. Ternan, Eds.), Vol. 1, p. 152. Chem. Institute of Canada, Ottawa, 1988.
40. Lacroix, M., Jobic, H., Dumonteil, C., Afanasiev, P., Breysse, M., and Kasztelan, S., *Stud. Surf. Sci. Catal.* **101**, 117
41. Mangnus, P. J., Riezebos, A., van Langeveld, A. D., and Moulijn, J. A., *J. Catal.* **151**, 178 (1995).
42. Parham, T. G., and Merrill, R., *J. Catal.* **85**, 295 (1984).
43. Kulharni, G. U., and Rao, C. N. R., *Catal. Lett.* **11**, 63 (1991).
44. Yoshimura, Y., Matsubayashi, N., Sato, T., Shimada, H., and Nishijima, A., *Appl. Catal. A* **79**, 145 (1991).
45. Matsubayashi, N., Shimada, H., Sato, T., Yoshimura, Y., Imamura, M., and Nishijima, A., *Fuel Process. Technol.* **41**, 261 (1995).
46. Yokoyama, Y., Yshikawa, N., Nakanishi, K., Satoh, K., Saito, T., Nishijima, A., Shimada, H., Matsubayashi, N., and Nomura, M., *Catal. Today* **29**, 261 (1996).
47. de Boer, M., van Dillen, A. J., Konigsberger, D. C., and Geus, J. W., *J. Phys. Chem*. **98**, 7862 (1994).
48. Startsev, A. N., and Kochubei, D. I., *Kinet. Catal.* **35**(4), 543 (1994).
49. Teo, B. K., "EXAFS: Basic Principles and Data Analysis," p. 101. Springer-Verlag, Berlin, 1986.
50. Ashcroft, A. T., Cheetham, A. K., Harris, P. J. F., Jones, R. H., Natarajan, S., Sankar, G., Stedman, N. J., and Thomas, J. M., *Catal. Lett.* **24**, 47 (1994).